Second-Order Memristor Based on All-Oxide Multiferroic Tunnel Junction for Biorealistic Emulation of Synapses

Anton Khanas, Christian Hebert, Loïc Becerra, Xavier Portier, Nathalie Jedrecy

ADVANCED ELECTRONIC MATERIALS
www.advelectronicmat.de

Second-Order Memristor Based on All-Oxide Multiferroic Tunnel Junction for Biorealistic Emulation of Synapses

Anton Khanas, Christian Hebert, Loïc Becerra, Xavier Portier, and Nathalie Jedrecy**

The brain has the ability to learn and evaluate as it receives and registers information. Signals between neurons are transmitted via synapses whose plasticity is modulated by usage. A bio-realistic electrical analog is a second-order memristor, where the short-term internal dynamics influence the long-term state. It is achieved here with an all-oxide multiferroic tunnel junction: $La_{0.7}Sr_{0.3}MnO_3$ / $BaTiO_3$ / $La_{0.7}Sr_{0.3}MnO_3$. Similar to the modulation of synaptic weight by stimuli, multi-levels of resistance may be encoded by mean of voltage pulses, on long time scale and in correlation with short-term effects. Neuromimetic learning functions are demonstrated: short and long-term potentiation/depression, paired-pulse facilitation/depression, spike-rate- and experience-dependent plasticity. The threshold frequency of pulse trains at which depression changes into potentiation depends on the previous activity, with a sliding effect as in neurobiology. The voltage pulses induce reversible changes of both dielectric polarization and oxygen vacancies distribution, generating transient trapped/detrapped charges at the two interfaces that govern the dynamic response. The resistance levels are determined by the final cationic ordering (the redox Mn^{3+}/Mn^{4+} ratio) at the two interfacial layers. The stimulation/relaxation dynamics are close to that in biological counterparts. Such memristors can be used in hardware artificial networks for advanced processing/storage of the information.

1. Introduction

The emulation of some functionalities of the human brain by artificial neural networks (ANNs) has been demonstrated with the "software" route. Even more sophisticated forms of learning are envisaged with the "hardware" implementation of electronic components, reproducing closer the behavior of neurons and biological synapses. Memristors are considered good candidates for emulating synapses, which constitute the interconnection between individual neurons.[1] Memristor is a two-terminal electronic device, the resistance of which can be continuously adjusted by use of external voltage pulses of appropriate amplitude/duration, while being stored nonvolatile.[2,3] These two characteristics mimic synaptic plasticity, that is the modulation of the transmission of signals ("spikes") transmitted from a pre-neuron to a post-neuron, and the conservation over time of the synapse state.

Learning consists in varying the "weight" (reinforcement or inhibition) of different synaptic contacts, through regulation by diverse biological molecular mechanisms. In terms of brain memory, the incoming information is stored short-term or long-term depending on stimulating conditions. In a "first-order" memristor, the conductance/resistance which figures the weight, is determined primarily by the voltage stimulation and the initial state. With such memristor, by use of voltage pulses or adequate voltage temporal profiles, a number of synaptic functions such as long-term potentiation/depression (LTP/LTD) and spike-timing-dependent plasticity (STDP) can be realized.[1] In real biological systems, the transmission of an electrical signal (spike) is carried out by the release of neurotransmitters into the synaptic cleft by a pre-neuron and the recapture of these by the post-neuron, via a complex sequence of events: opening at the level of cell membranes of channels permeable to K^+, Na^+,[4] Ca^{2+} ions,[5] fusion of vesicles,[6] activation/accumulation of AMPA and NMDA receptors,[7] etc. (**Figure 1**a). In particular, the sensitivity of the synaptic weight to stimuli is regulated by the concentration of Ca^{2+} ions, which rises under the effect of a spike, then decays exponentially over a range of 10^{-3}–100 s.[8–10] This effect provides the transient conditions for transmission tuning on a short time scale, with or without long-term effects. Similar synaptic behavior can be achieved with a "second-order" memristor, where the conductance/resistance value results

A. Khanas, C. Hebert, L. Becerra, N. Jedrecy
Institut des Nano Sciences de Paris (INSP)
CNRS UMR 7588
Sorbonne Université
4 Place Jussieu, Paris Cedex 05 75252, France
E-mail: khanas@phystech.edu; jedrecy@insp.jussieu.fr
X. Portier
Centre de recherche sur les Ions
les MAtériaux et la Photonique (CIMAP)
CEA
CNRS UMR 6252
ENSICAEN
Normandie Université
6 Boulevard Maréchal Juin, Caen 14050, France

The ORCID identification number(s) for the author(s) of this article can be found under https://doi.org/10.1002/aelm.202200421.

DOI: 10.1002/aelm.202200421

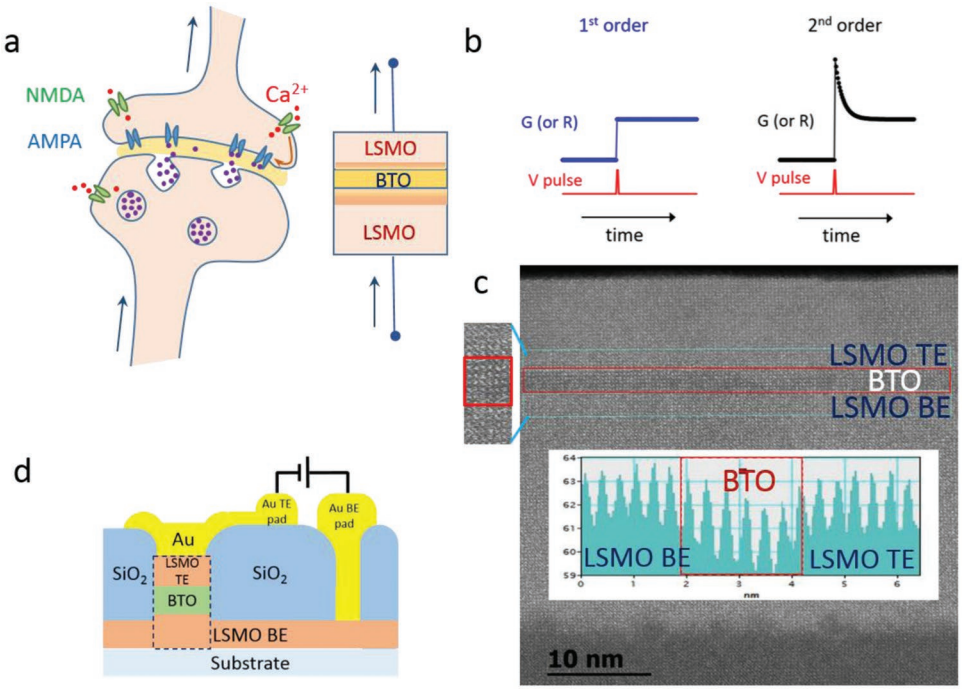

Figure 1. Memristor for synapse emulation. a) Schematic of synapse and memristor. b) Conductance (or resistance) of 1st or 2nd order memristor in response to voltage pulse. c) HAADF-STEM cross-section of the junction with zoom on the left. Inset shows the intensity profile of the highlighted area to accurately define the interfaces. d) Sketch of the device after the lithography process.

from both the external stimulation and "instant" internal states.[11–13] The dynamics of internal states is depending on a second variable (or a set of second variables) which does not directly control the conductance/resistance but will manifest itself indirectly through activity-dependent changes (Figure 1b). Whereas the conductance G of a first-order memristor is determined solely by a state-variable s_1 which is varied by the input voltage V (the derivative of s_1 by time is a function of V and s_1), in a second-order memristor, the derivative of s_1 by time additionally depends on a second variable s_2, although s_2 does not directly determine the G value. In other words, s_2 regulates the dynamic process of s_1 and enables activity-dependent modulation of G. Such memristors would allow for more bio-realistic simulation of the synaptic behavior, and hence increase learning performance of hardware ANNs.[14]

Different mechanisms/devices have been proposed for the second-order adjustment of the conductance of a memristor. The applied voltage can induce heating of the device, which will assist the formation of conductive filaments[11]; voltage modulates the mobility of oxygen ions which will also aid in the formation of conductive filaments[12]; silver nanoclusters embedded in dielectric films may play the role of the Ca^{2+} ions.[13] Another important implementation of the second-order memristor is the metal/ferroelectric (FE)/semiconductor-substrate structure, where a FE tunnel junction (FTJ) is realized. The polarization switching in the FE by voltage modulates the transmission through the tunnel barrier and therefore the resistance, while the density of transient screening charges at the interfaces determines the dynamic response of the device.[15,16]

Junctions based on a FE thin film are a much-studied field of research[17] due to the tunneling electroresistance (TER) as well as the (first-order) memristive effects that may result from the inherent switching by voltage of FE domains. The perovskite FE oxides $BaTiO_3$ (BTO),[18–23] PZT,[24] $BiFeO_3$,[25] and the $Hf_{0.5}Zr_{0.5}O_2$ oxide[16,26–27] have been particularly studied. The epitaxial growth process of FE BTO is well established whether on substrates like $SrTiO_3$[28] or on conductive films like $La_{1-x}Sr_xMnO_3$ (LSMO, $x = 0.2 - 0.33$).[29] LSMO belongs to the class of ferromagnetic (FM) half-metals, where conductivity and magnetism are intimately linked by a double-exchange mechanism within Mn^{3+}–O^{2-}–Mn^{4+} chains.[29,30] The three-layer LSMO/BTO/LSMO system is thus of particular interest since it combines FE and FM properties (it may be considered as a type-I multiferroic), while adding charge/orbital degrees of freedom.[31–37] It can be used as a FTJ, as a magnetic tunnel junction, or as a multiferroic tunnel junction, for independent memory capacities,[31,32] memristive properties,[35] magnetoelectric coupling.[34] However, the interface chemistry must be carefully controlled to ensure the required device properties.

It has been shown[32,33,38] that the mixing of ions at the BTO/LSMO interface significantly modifies the properties of the interfacial layers of the LSMO film. The Mn^{3+}/Mn^{4+} ratio can deviate from the optimal point, which leads to the breakdown of the double exchange mechanism along the chains; this, in turn, induces a metal-insulator transition (MIT) in the LSMO interfacial layers. An equivalent effect has been demonstrated via the insertion of a thin layer of $La_{1-x}Ca_xMnO_3$ between BTO and LSMO.[39] Remarkably, the MIT effect at LSMO interfaces can be made controllable: voltage application can either induce migration of oxygen vacancies, which will change the redox nature of the chains,[38] or induce BTO FE switching, which will likewise change the electrostatic charges at the interfaces.[40,41]

The LSMO/BTO/LSMO system thus provides the interplay ground between BTO FE ordering and charge ordering from Mn cations. Nevertheless, it should be noted that so far for BTO-based systems only first-order memristors have been reported: at room temperature with metallic top electrodes,[18–20] and at temperatures below 80 K for LSMO/BTO/$CoFe_2O_4$[21] and LSMO/BTO/LSMO junctions.[34,35]

In this work, we realized multiferroic LSMO/BTO/LSMO second-order memristors, which display at room temperature bio-realistic synaptic functionalities: short- and long-term potentiation/depression (STP/STD and LTP/LTD), paired pulse facilitation/depression (PPF/PPD), spike rate-dependent plasticity (SRDP), and experience-dependent plasticity. We attribute this behavior to the reversible modification, by the applied voltage pulses, of the two LSMO/BTO and BTO/LSMO interfacial layers, via short-term and long-term evolution of the interfacial mobile and electrostatic charges, as induced by the polarization of FE BTO and the accumulation/depletion of oxygen vacancies.

2. Results and Discussion

2.1. Multilevel Resistive Switching of the LSMO/BTO/LSMO Junction

2.1.1. Sample Description and Device Fabrication

The LSMO/BTO/LSMO heterostructures were grown by pulsed laser deposition (PLD) on $SrTiO_3$ substrates with a post-growth annealing in O_2 atmosphere; details on the growth procedure may be found in our previous study.[38] The crystalline quality of the layers is confirmed by X-ray analysis (Figure S1, Supporting Information) and high-angle annular dark-field scanning tunneling electron microscopy (HAADF-STEM). The junction cross-section shown in Figure 1c confirms the cube-on-cube epitaxy of the LSMO and BTO layers, and the abruptness of the two interfaces. The thicknesses of the layers are 9 nm/2.3 nm (i.e., 6 unit cells)/22 nm for top LSMO/BTO/bottom LSMO, respectively. An important feature is the asymmetry of the two interfaces, highlighted through the integrated intensity profile starting from the bottom electrode (BE) up to the top electrode (TE). The lower interface is more gradual than the upper one. We know that the cationic intermixing, which occurs between BTO and LSMO, results in a chemical reduction of the Mn ions, from Mn^{4+} (Mn^{3+}) toward Mn^{3+} (Mn^{2+}).[32,37,38] Electron energy loss spectroscopy (EELS) analysis at the Mn $L_{2,3}$ edge (Figure S2, Supporting Information) confirms that this Mn reduction may indeed take place at both interfaces, but with a prevalent effect for the bottom one. The asymmetry of the LSMO/BTO/LSMO junction has also been reported in other studies.[32,34] It may naturally be explained by the stacking sequence of AO and BO_2 atomic planes in the growth of the ABO_3 perovskite. Putting aside the ion-mixing effects, one expects to have BaO on MnO_2 at the lower interface and (La,Sr)O on TiO_2 at the upper interface.

The FM ordering of each LSMO layer (bottom and top) has been confirmed by the magnetic measurements (Figure S3, Supporting Information), where the two components are clearly identified.

The plain films were HCl-etched down to the BE through windows patterned by photolithography, letting square pillars of 100 µm in lateral size on the sample. For electrical isolation of the devices, the inter-pillar area was covered with 200 nm thick SiO_2 by magnetron sputtering, with the access to the TE of the pillars being organized through lift-off procedure (Figure 1d). Finally, 250 nm thick Au layer was thermally evaporated, and the TE of pillars connected to 400 µm square contacting pads, located on SiO_2 for safe wire bonding or probe landing. Access to the common BE was done through an Au window in SiO_2 down to the etched surface level. In all electrical measurements, the TE of the measuring device was connected to the ground, while the potential was applied to the BE.

Local piezoresponse force microscopy (PFM) measurements on uncovered LSMO/BTO/LSMO pillars (Figure S4, Supporting Information) reveal the presence of a built-in electric field (imprint of ≈ +0.5 V). The native BTO FE polarization is oriented downwards. Its switch to upwards may be realized for voltages higher than ≈ +0.6 V but this upwards configuration is not stable when the voltage is turned off. This supports the view of an as-grown state with a downwards polarization stabilized by the electron accumulation at the BE which results from the increased amount of Mn^{3+} with respect to Mn^{4+} at this interface.

2.1.2. Resistive Switching Measurements

The current-voltage (I–V) measurements were performed in a conventional two-step sequence: V alternately takes V_{write} and V_{read} values, the V_{write} values following a triangular profile while V_{read} is fixed. After each "write" voltage, the resistance state of the device is tracked through the "read" voltage of 50 mV, according to $R = V_{read}/I_{read}$. The duration of all voltage pulses was 1 ms. A typical result of such measurements is presented in **Figure 2**. The $I(V_{write})$ dependence demonstrates the diode-like behavior of our junction with a marked hysteresis region in the (blocked flowing) positive bias range (Figure 2a). A faint hysteresis is also present in the $V < 0$ range which may be seen using the log scale (see the full pinched hysteresis in Figure S5).

The related $R(V_{write})$ curve appears as a stable hysteresis cycle between two well-defined resistance states (Figure 2b). The upper branch of the $I(V)$ curve in the $V > 0$ region, i.e., the branch with the higher slope near 0, corresponds to the growing resistance branch of the $R(V)$ curve. It represents the switching from a low resistance state (LRS), set with −3.5 V consistently from various initial levels, to a high resistance state (HRS). The HRS level depends on the highest positive applied voltage and is reproducible; for each maximum positive voltage, three cycles were performed, all coinciding. In all $R(V)$ curves, switching from LRS to HRS starts at ≈ +1.5 V and the $R(V)$ curve follows the same path whatever the value of the maximum positive voltage, while switching from HRS to LRS starts at ≈ −0.8 V and leads to a single LRS level at −3.5 V with different curve steepness depending on the initial HRS level. In other words, any intermediate resistance state may be reached starting from a lower resistance level by a fixed value of positive voltage, while starting from a higher level, the value of necessary negative voltage will depend on this initial level. Using a longer time duration of write/read pulses will reduce

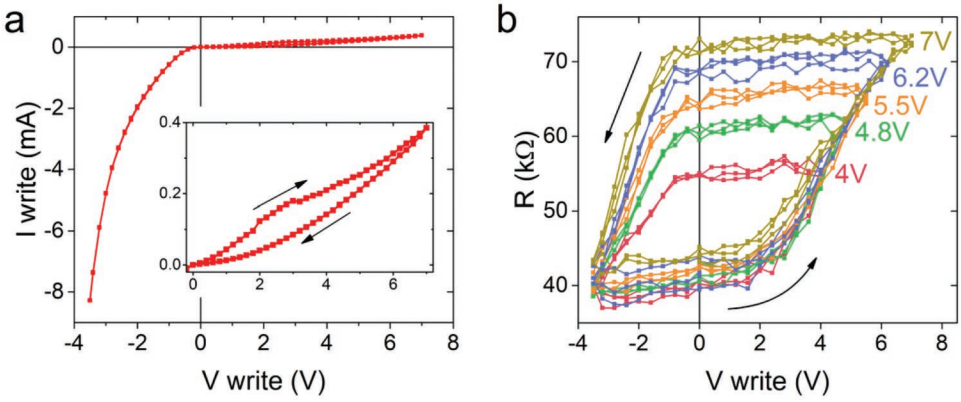

Figure 2. Resistive switching of a 100 µm device. a) $I_{write}(V_{write})$ curve and b) multilevel $R(V_{write})$ curves, cycling between −3.5 V and different V_{max} values and vice versa. For the $I(V)$ curve, a single cycle with +7 V maximum voltage is shown for clarity (all other curves follow the same path). Inset in (a) displays the zoomed-in hysteretic region of the $I(V)$ curve. Arrows indicate the voltage sweeping order.

somehow the width of the hysteresis loop but not its shape (Figure S6, Supporting Information).

Since we deal with two nonequivalent interfaces from structural/chemical point of view (see Section 2.1.1), the diode-like shape of the $I(V)$ curve is in accordance with a *p-n*-like junction where the *p* (*n*) side would correspond here to the TE (BE). This goes in line with a BE more reduced from a chemical point of view than TE and where the ratio Mn^{4+}/Mn^{3+} of BE is lowered with respect to ideal value, with the eventual presence of Mn^{2+} cations. Indeed, the Mn^{3+} and Mn^{2+} ions from the BE may act as electron donors for electrical transport through the BTO up to TE. Concerning the resistive switching process by itself, we underline that no electroforming process is required, that the transitions between HRS and LRS are continuous, and that the $I(V)$ or $R(V)$ curves are highly reproducible cycle after cycle. This differs from resistive switching attributed, in junctions of different types, to the formation/disruption of transverse conductive filaments, whatever the nature of the latter.[42] We rather deal in our case with continuous variations of the charge repartition at the two interfaces, whether it results from BTO dielectric polarization switch or drift of oxygen vacancies with an applied electric field or from both mechanisms.[43] The LRS corresponds to the native state where polarization points downwards but the resistive switching to HRS cannot be explained in our case on the basis of a fraction of down to up switched domains, since up domains are not stable. The new repartition of screening charges at the two LSMO interfaces in the HRS, which succeeds to the removal of the electric field (polarization switched back), is determining by itself the final resistance level. The polarization rather acts as a second-order variable influencing for short time the system state, as it will be shown later.

We have analyzed the $I(V_{write})$ curve in the low voltage range according to the direct tunneling model in the two HRS and LRS situations (Figure S7, Supporting Information). The fit-extracted barrier thickness is close to 4.2 nm in the two cases whereas the potential barrier heights at BE and TE sides are respectively found equal to 4.7 and 0.2 eV in the LRS case, and equal to 5.1 and 0.1 eV in the HRS case. The higher value found for barrier thickness with respect to the expected one is probably resulting from the existence of the ion intermixing at the interfaces.

2.1.3. Switching Dynamics and State Retention

The dynamics of resistance state switching were assessed in detail. The same two-step write-read sequence was used, with the same pulse duration and reading voltage value as for previous measurements. The application of a series of pulses demonstrates the continuous character of the switching and its reproducibility (**Figure 3**). First, a series of writing pulses with various voltage values from +1 to +7 V (Figure 3a) or from −1 to −3.5 V (Figure 3b), was applied after 250 prepulses of the opposite polarity used to prepare the initial state. It is clearly seen that different voltage values of the writing pulses induce different final resistance states, which are reached nonlinearly and more or less easily with the number of pulses increasing. Next, a series of −3.5 V pulses followed by a series of +5 V pulses (Figure 3c) were applied, using different sequences where the number of +5 V pulses doubles at each round. Similar measurements were done with +7 V pulses followed by −2 V pulses (Figure 3d). The couples of voltage values were selected to prepare the same reference state, as quickly as possible, with the series that have a fixed number of pulses (−3.5 V and +7 V, respectively, corresponding to the steepest switching curves of Figure 3a,b), as well as to demonstrate the gradual switching with the series where the number of pulses is doubled at each sequence (+5 V and −2 V, respectively, corresponding to the curves of intermediate steepness in Figure 3a,b). The switching paths during any series with doubled number of pulses are well reproduced, showing the good reliability of the device.

Finally, we investigated the long-term retention of the resistance states (Figure S8, Supporting Information). Starting from different levels, we measured the resistance value every 10 s during 10 min, with 50 mV and 1 ms reading pulses. All settled multi-level states are satisfactorily stable. The endurance of our device was assessed by the measurement of 50 successive $I(V)$ cycles and 10^5 HRS-LRS switches (Figure S9–S10, Supporting Information).

Essentially, the measurements of this section are a manifestation of LTP/LTD, a basic feature of plasticity. By selecting an appropriate voltage/number of the writing pulses, it is possible to cover a wide range of accessible resistance states, i.e., potentiated or depressed synaptic weights.

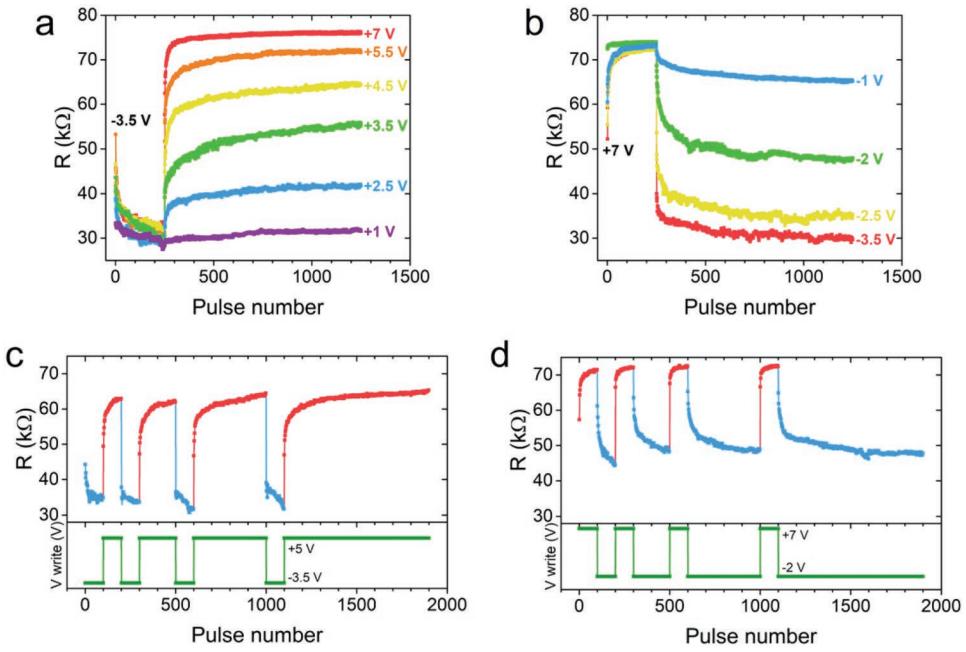

Figure 3. Switching dynamics and saturation. a,b) Multi-level resistance states set with (a) positive and (b) negative writing pulses, after 250 prepulses of (a) −3.5 V and (b) +7 V. c) Pulse series with −3.5 V then with +5 V, repeated in sequences where the number of pulses in the second group doubles at each round. Reading was made with 50 mV and duration of 1 ms, the period of write pulse application being 0.5 s. Red and blue colors are used for differentiating potentiation from depression. d) The same with +7 V, then 2 V.

2.1.4. Relaxation Dynamics of the Resistance State After a Single Pulse

For further knowledge of the memristor dynamics, we investigated the effects of a single write pulse by following the relaxation of the state after this isolated stimulus. In the beginning, the state (any intermediate level) was read with a number of 50 mV pulses, then a single write pulse of +6 V (red squares) or −2 V (blue squares) was applied, followed again by reading pulses (**Figure 4**a). The duration of all pulses was kept at 1 ms, the pulse application period being ≈260 ms. It is found that the resistance increase (decrease) generated by the single +6 V (−2 V) pulse excitation is rapidly followed by a decay (rise) with time to a final level, which stays however higher (lower) than the initial (Figure 4a). Stabilization of the resistance state after the negative voltage pulse application is achieved in less than 10 s, while for the positive voltage pulse it takes ≈50 s, and two very different decay rates are evidenced (abrupt decrease followed by softer one). These measurements demonstrate the ability of our device to tune its state on a long-term timescale after a single pulse excitation, as well as they reveal temporary states on a short-term timescale. This behavior is analogous to the long-term and short-term synaptic potentiation/depression effects, which are responsible for the long- and

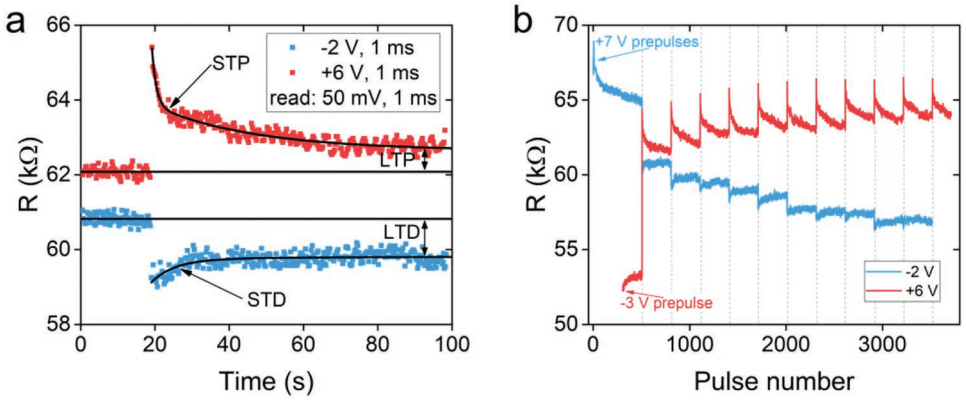

Figure 4. Relaxation dynamics from potentiated/depressed states. a) Relaxation of the resistance state, read with 50 mV, after excitation with a single pulse of + 6 V (red squares) or – 2 V (blue squares). b) Multiple resistance levels are achieved by repeating the same writing pulses, identified by the vertical dotted lines, each followed by reading tracked with time.

short-term memory and learning processes. Notably, the shape of the resistance curves following pulse stimulation very closely resembles that of excitatory postsynaptic potential (EPSP) slope or current measured from the visual cortex, hippocampus, and other regions of the brain.[44–47]

The same stimulation/relaxation procedure with +6 V/50 mV or −2 V/50 mV was repeated sequentially (Figure 4b). Note that a pre-writing with either one −3 V pulse (red line) or five +7 V pulses (blue line) was done to set the initial state. The application of successive +6 V (or −2 V) writing pulses, each one succeeding to the time decay (rise) of the preceding sequence, leads to a step-like resistance evolution. In this single-pulse repeated way, resistance levels can be tuned quasi-continuously while stabilized into quasi-persistent states.

At this stage, we must emphasize the following point. We use the label P of potentiation (D of depression) for an increase (decrease) of the resistance state which is considered in our case, oppositely to conventional conductance, as a measure of the synaptic weight. Indeed, we have discussed in Section 2.1.2 the fact that the LRS obtained after the application of sufficient negative voltage is the more stable state, that is the ground state of the memristor. Positive voltages lead to excited HRS states. It is thus natural to treat the increase of the device resistance as synaptic potentiation and it's decrease as depression.

Our relaxation measurements, while giving another proof for the presence of LTP/LTD, highlight the presence of STP/STD effects. From Figure 4a, it is obvious that the switching with negative voltage from any intermediate level to a lower resistance state needs lower stabilization time and is of lower magnitude, than the reverse switching with positive voltage. One may note that the STD → LTD raise involves a single time constant $\tau = 7$ s while the STP → LTP decay involves two-time constants $\tau_1 = 1$ s and $\tau_2 = 27$ s. In addition, we observe that the voltage sign sequence between two successive pulses has a strong influence (Figure 4b). Changes are amplified when $V > 0$ succeeds to $V < 0$ (or the reverse). From these features, we infer that stimulation by a positive pulse leads both to oxygen vacancy drift (BE → TE) and FE polarization reversal (down → up). When voltage is turned off, part of oxygen vacancies diffuses back and polarization returns down. Stimulation by a negative pulse only induces the drift of oxygen vacancies (followed by their diffusion). The time constants of such processes are compatible with our findings.[48,49]

In accordance with the resistive switching mechanism suggested in Section 2.1.2, we propose the following explanation of the time-dependent behavior observed. During the positive voltage application (to the BE), the FE polarization is switched upwards and oxygen vacancies ($V_O^{\cdot\cdot}$) are attracted toward the top LSMO/BTO interface. In response to each process, the occurrence of a redox reaction (Equation 1 or 2, respectively) may be considered:

$$Mn^{3+} \rightarrow Mn^{4+} + e^- \quad (1)$$

$$Mn^{3+} + \frac{1}{2}V_O^{\cdot\cdot} \rightarrow Mn^{4+} + \frac{1}{2}O^{2-} \quad (2)$$

increasing in each case the Mn^{4+}/Mn^{3+} ratio at the top interface and making this interface more conductive

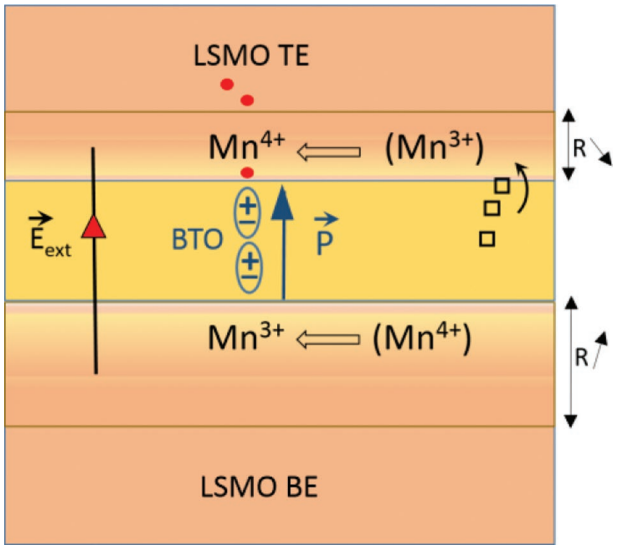

Figure 5. Schematic sketch of the LSMO/BTO/LSMO memristor with a $Mn^{4+} \leftrightarrow Mn^{3+}$ redox reaction occurring at both interfaces under application of a positive voltage to BE. The BTO polarization is switched upwards and the oxygen vacancies (squares) migrate upward. The resistance of BE increases while that of TE decreases.

(see **Figure 5**). Reversed phenomena are at play at the bottom interface. As our measurements show an increase in the junction resistance under positive voltage, the BE interface has a prominent effect on the final value of the resistance. When voltage is removed, the polarization switches back to down orientation, and oxygen vacancies are generated at the top, resulting in a new equilibrium of the charges localized at Mn species. The final distribution of charges trapped at interfaces is determining the Mn^{4+}/Mn^{3+} ratio and the long-term resistance with respect to starting value.

2.2. Second-Order Memristive Effects

2.2.1. Justification and Prerequisites

It was shown in the previous section that an excitation with a positive single voltage pulse always results in a resistance jump, followed by its decay to some level, defined by the initial resistance state. This brings up the following question: in case a second pulse is applied during the resistance decay following a first pulse, what would be its effect: cumulative or enhanced? In other words, does the resistance depend on the interval between consecutively applied writing pulses? (**Figure 6**a). A variety of amplification effects has been discovered in the performance of biological synapses.[8–10] Conventionally, they are well explained on the basis of the second-order model described in the introduction.[11,12,50] In the biological synapse, the transmission of spikes is determined by the fusion of vesicles and fixation of neurotransmitters to AMPA receptors. The latter act as Na^+, K^+ ion channels and mediate the propagation of electrical signals. An increased clustering of AMPA receptors is induced by activation of NMDA receptors, highly permeable to Ca^{2+} ions.[51,52] In a simplified view, AMPA receptors may

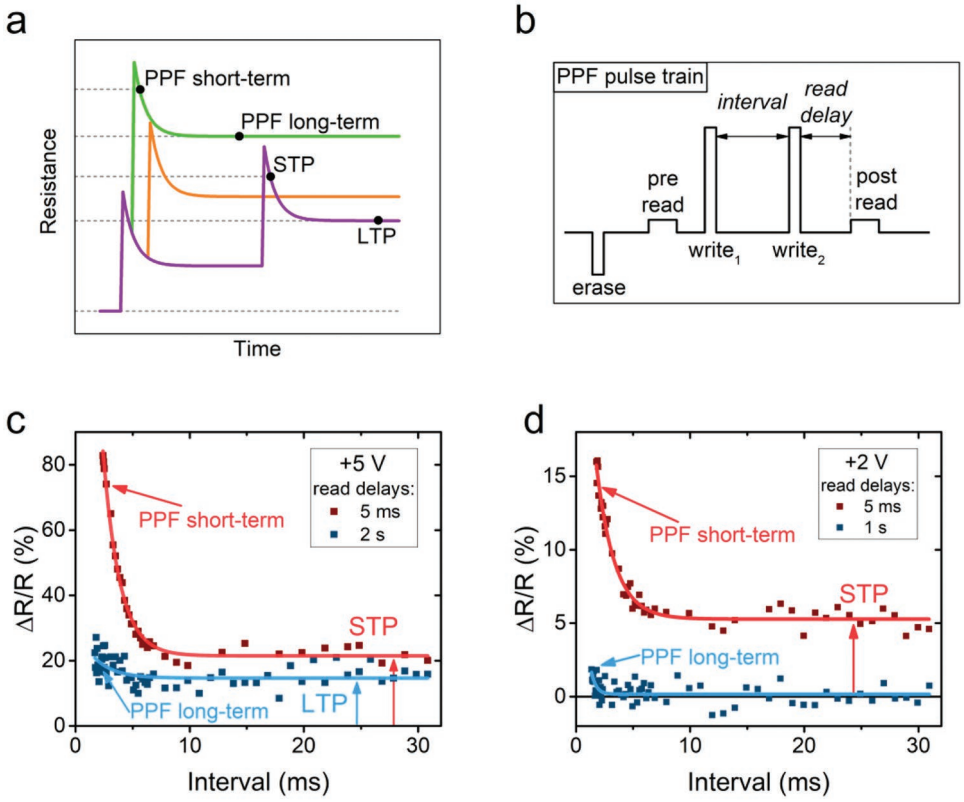

Figure 6. Facilitation is induced by a pair of pulses. a) Sketch of cumulative versus enhanced effects. b) Sketch of the pulse train with an interval between write pulses and a post-read delay that both will be varying. c,d) Relative change of the junction resistance after the paired-pulse stimulation with respect to the initial resistance value (R_{pre}), as a function of the time interval between two writing pulses of (c) +5 V and (d) +2 V. Red (blue) curve corresponds to short (long) postread delay.

be considered as a first-order variable for synaptic plasticity while NMDA-mediated Ca^{2+} ions act as a second-order variable. When a spike is fired by a presynaptic neuron, besides the possible direct increase of the synaptic weight, the concentration of Ca^{2+} instantly rises, but immediately starts to decay. The importance of the phenomenon is that Ca^{2+} content contributes to the ionic conductance of the synapse by itself, and, moreover, increases the modulation effect of the spike if the latter is fired when the Ca^{2+} concentration is still high. Hence, the time-dependent effects are explained by the temporal rise and decay of the Ca^{2+} content.

In the case of our LSMO/BTO/LSMO memristor, we defined the device resistance as the synaptic weight. The factor that determines long-term resistance (first-order effect) is the degree of reduction/oxidation of the two interface layers at equilibrium, as a result of second-order effects: i) oxygen vacancy drift and polarization switch induced by voltage (Figure 5), then of ii) vacancy diffusion and FE depolarization. Trapping/de-trapping of charges from LSMO layers accompanies these stimulation and relaxation processes. The LSMO/BTO/LSMO memristor temporal response during and after stimulation is, as in biological systems, dependent on the dynamics of second-order variables. Now we proceed to the observation of specific second-order synaptic functions.

2.2.2. Paired Pulse Facilitation

In neuroscience, the PPF (Figure 6a) is a prominent feature of short-term EPSP enhancement due to Ca^{2+} cations. To observe it, a pair of spikes (writing pulses in the memristor case) should be applied at various time intervals. The effect of a single pulse on the synaptic weight may vary (excitation, depression, with possibly no long-term result at all), but a pair of pulses will have a facilitation effect with a strong dependence on the interval duration between the two pulses. To investigate the effect, trains of five pulses were applied (Figure 6b): first, an "erase" pulse prepares the system in a given initial state; second, a reading pulse (pre-read) of 50 mV, 0.1 ms measures the initial resistance R_{pre} of the junction; third and fourth, a pair of writing pulses is sent with a fixed time interval; fifth, a reading pulse (post-read) is applied to measure the final R_{post} resistance state. The delay before reading this final resistance was varied: 5 ms delay corresponds to a short-term measurement, while 1 or 2 s corresponds to a long-term measurement. The result of the paired stimulation is shown as the relative resistance change $\Delta R/R = (R_{post} - R_{pre})/R_{pre}$ for each pulse train with a fixed interval, this interval having been varied between 1.7 and 32 ms. Two sets of measurements were performed: with +5 V pulses (Figure 6c) and +2 V pulses (Figure 6d), both pulses lasting 70 µs. The very initial erase voltage was selected with the

condition to keep the R_{pre} value constant throughout the whole measurement; its value was −3 V and −2 V, respectively.

Focusing on the +5 V paired pulses measurement (Figure 6c), it is seen that the $\Delta R/R$ value, on both short- and long-term timescale of postreading, indeed depends on the time interval between the writing pulses, i.e., the synaptic weight increase is facilitated at shortest intervals and facilitation decreases as interval increases. This demonstrates that the short-term potentiation with paired pulses is higher than from repeated individual pulses. The significantly smaller PPF long-term change (for longer read delay) with respect to the short-term one (for shorter read delay) illustrates the time-dependent second-order dynamics. The facilitation induced by pulse pairing decreases from more than 80% to 25% at the smallest interval (1.7 ms), while the facilitation slightly decreases from 20% to 15% at the largest intervals. As for the case of +2 V pair of pulses (Figure 6d), it is seen that on a long-term time scale, it induces no resistance modification: $\Delta R/R$ fluctuates around 0. However, on the short-term time scale, a short interval between paired pulses still induces facilitation up to 15%, while at 7 ms interval and higher the change is only around 5% which corresponds to the STP of individual +2 V pulses. This result shows that even when sufficiently low voltage pulses are applied, so that no LTP is induced, the short-term PPF may be significant.

2.2.3. Spike Rate-Dependent Plasticity and Experience Dependent Plasticity

The second-order functionalities may be achieved in a more general way using pulse trains of different rates (SRDP) instead of a simple pulse pair. This approach better mimics the biological situation of a neuron receiving multiple spikes from other neurons, the averaged synaptic weight depending both on the number of pulses (spikes) and their frequency. At high frequencies of the pulse train (i.e., using short time intervals between individual pulses) the synaptic weight should become higher, similarly to the PPF effect. Conversely, at low frequencies of the excitation, a synaptic depression, similarly to PPD effect, should be observed. The measurement started with the application of a series of writing pulses (+5 V, 100 µs) at two frequencies: 150 Hz (300 pulses per series) and 1 Hz (20 pulses per series). The results are displayed in Figure S11, Supporting Information through the synaptic weight (w) modification. The w values were extracted from the I_{write} current measured during each pulse, which is correlated with the device resistance; as was demonstrated in Section 2.1.2, the resistance change is accompanied by the change of the writing current of the opposite sign, which is happening continuously. The calculation details are described in Figure S12, Supporting Information. One observes that indeed the high-frequency input induces the synaptic potentiation, while the low-frequency input induces depression whereas the same voltage value is used.

We must note here that SRDP in our memristor emerges as the consequence of short-term resistance elevation that naturally tends to the decay, while with sustained external excitation the system is not allowed to relax completely and its state is instead prolonged. By using the SRDP, we are able to induce the synaptic depression without the need of application of a voltage with opposite polarity. This behavior of our memristor proves to be in good agreement with the functioning of its biological counterpart, since the cortical synapses are also continuously being subjected to a variety of inputs from the environment when the owner organism is active. Even in the deprived conditions, the cells are provided with a certain noise level, which is not letting full relaxation through short-term dynamics.[53]

The biorealistic functioning of our memristor is deepened by the implementation of experience-dependent SRDP measurements. This manifests in the dependence of the synaptic weight not only with the frequency of the stimulation, but also with the history of the frequencies of previous stimulations. It was shown that the synapses can be both potentiated or depressed with the same spike trains, depending on the previous changes in the system.[12,45,46,51,54] If a pulse train at some frequency is applied after a lower frequency train, it induces strengthening of the synaptic weight. Oppositely, when the same pulse train is applied after a faster stimulation, it induces weakening. The experience-dependent SRDP effect in our junction is illustrated in **Figure 7**a. The +5 V, 100 µs pulses were applied at three different frequencies: low, intermediate, and high (5, 50, and 120 Hz, respectively) with different number of pulses (5, 50, and 100, respectively). The lowest (highest) frequency train always induces synaptic depression (potentiation), without any dependence on the order of pulse train application. For the intermediate frequency (50 Hz) train, the sign of the synaptic modification depends on the frequency of the previous train: if it follows the low frequency (5 Hz) train, the weight gradually increases; otherwise (120 Hz), the weight decreases. The extraction of each relative weight modification $\Delta w/w$ throughout each pulse train (Figure 7b) shows the consistent and reproducible change values from train to train, starting from the first 50 Hz train.

Another experience-dependent functionality is demonstrated when each pulse train is prepulsed with a train at some fixed frequency, the latter being varied. Frequencies of the pulse trains were swept in the range of 1 to 580 Hz in the ascending order, while before each train at a particular frequency, a prepulsing was made using either 20, 50, 100, 200, or 400 Hz frequency. All the trains consisted of 100 pulses (+5 V, 100 µs). The weight changes during each pulse train were extracted and are given in the form of five curves, each curve corresponding to a fixed pre-pulsing frequency (Figure 7c).

The SRDP extracted curves prove to be dependent on the pre-pulsing frequency, what manifests in the shift of the curves. Higher pre-pulsing frequencies result in a greater fraction of trains with lower frequency producing synaptic depression. For a given pre-pulsing frequency, the frequency at which the synaptic modification is zero is called the "threshold frequency". The values of threshold frequency are well correlated with pre-pulsing frequency values (Figure S13, Supporting Information).

These experience-dependent plasticity measurements were inspired by the Bienenstock–Cooper–Munro (BCM) theory of cortical plasticity.[53,55,56] In the BCM framework, plasticity is controlled solely by postsynaptic activity as determined by presynaptic spike. The starting assumptions of the model (purely theoretical at the moment of its publication[56] and later confirmed[5,7] upon the discovery of Ca^{2+} dynamics) lead to the direct prediction of rate-dependent plasticity with a sliding threshold

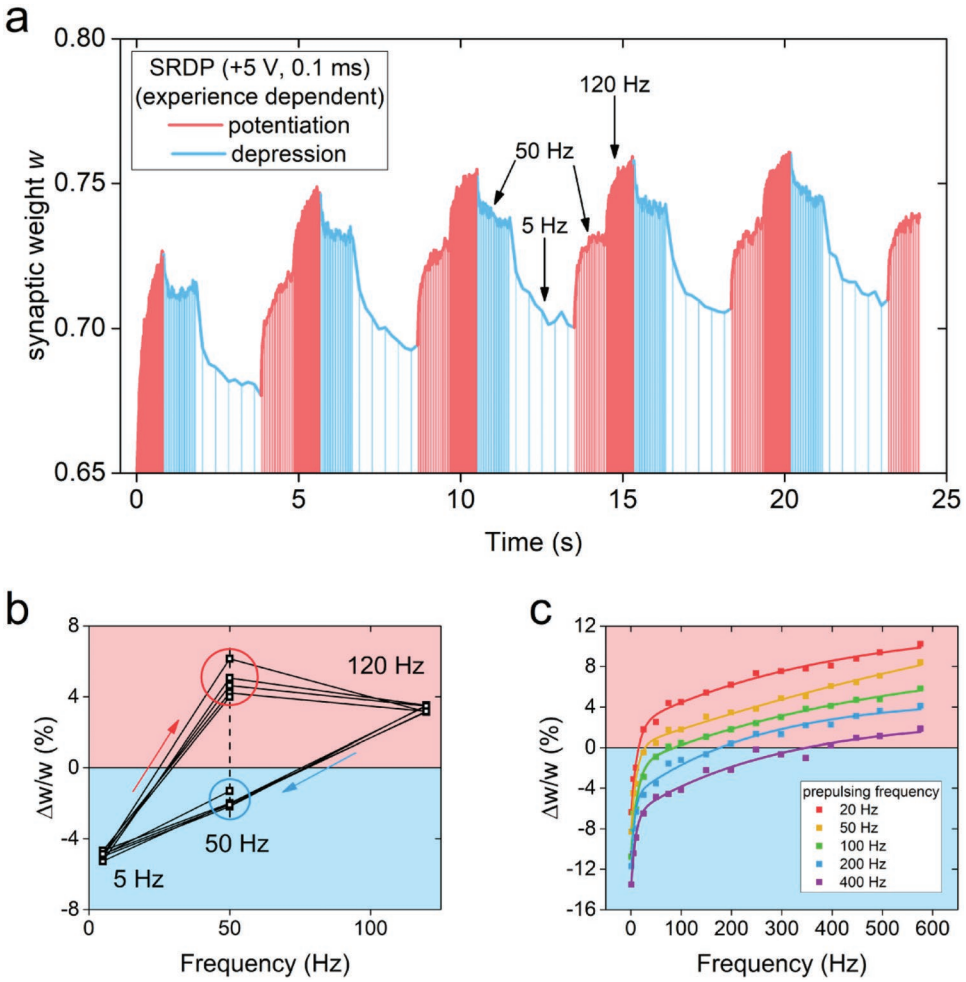

Figure 7. Historical dependence of synaptic plasticity induced by pulse trains of different frequencies. a) SRDP measured with different frequency orders of the successive trains, attesting of experience-dependent plasticity. Potentiation (depression) areas are indicated with red (blue) lines. Every second drop line was skipped for clearer presentation. b) The relative synaptic modification during a pulse train at a given frequency, extracted from each train considered in (a). c) Frequency dependence of the relative synaptic change during a pulse train which was preceded by a prepulse train with different frequencies, as given in the legend. Same number of pulses (100) was used for all trains.

feature, a manifestation of experience dependence. Various frequencies of the prepulsing train make an analogy to the various visual stimulation/deprivation conditions, which tune the threshold sensitivity of the synapses in the visual cortex.

The SRDP emulation requires a second-order memristor. In a different way, the effects of pre- and postsynaptic activities on a synapse, as a function of their timing, may be emulated by STDP experiments, whether the memristor is first- or second-order. A presynaptic stimulus (with a convenient profile in the case of a first-order memristor), followed by a postsynaptic stimulus (overlapping with it), should result in LTP whereas reversing the order of stimuli should result in LTD. The STDP measured in the conventional first-order fashion is given in Figure S14, Supporting Information. The STDP performed in a purely second-order fashion (i.e., the pre and post spikes were simple rectangular voltage pulses and the temporal behavior was thus induced by the inherent memristor dynamics) is provided in Figure S15, Supporting Information.

3. Conclusion

We have demonstrated the implementation of a second-order memristor, based on a multiferroic LSMO/BTO/LSMO tunnel junction. Dynamic modification of the two LSMO/BTO and BTO/LSMO interfaces through their redox Mn^{4+}/Mn^{3+} ratio, is suggested being the basis of long-term and short-term resistance tuning. It results both from BTO dielectric polarization switching/relaxation and oxygen vacancies drift/diffusion. The short-term and long-term coupled responses of our memristor have great similarities with neuronal behavior. Important features for biorealistic emulation of synapses have been observed and investigated, such as STP/STD, LTP/LTD, PPF/PPD, SRDP, and experience-dependent plasticity. We believe that our results broaden the understanding of second-order memristor functionalities for future implementations in neuromorphic networks and make a step toward the future realization of hardware ANNs.

4. Experimental Section

PLD Growth: The PLD growth was made with a frequency quadrupled Nd:YAG laser (wavelength 266 nm, 10 Hz repetition rate). Commercial BTO and LSMO targets were used. The films were grown at a substrate temperature of 600 °C, in a 10^{-2} mbar oxygen atmosphere, with a laser fluence of 100 mJ cm^{-2}. The samples were cooled at a rate lower than 5° min^{-1}. To improve crystallinity and ensure oxygen stoichiometry of the oxide layers, the samples were annealed post-growth at 800 °C in a 100 mbar oxygen atmosphere for 30 min.

Electric Measurements: All the electrical measurements were performed with a Keithley 2635B source measure unit (SMU) at the ambient conditions, using Cascade Microtech micromanipulators. Control over the SMU was organized via self-developed programs.

TEM: The atomic structure was analyzed by STEM using a double-corrected cold FEG ARM200F JEOL microscope, equipped with a HAADF detector. The microscope was operating at 200 kV; an EELS (QUANTUM ER from GATAN) was used to analyze Mn valence states. The TEM lamella was prepared by a focused ion beam (FIB) system (FEI HELIOS Nanolab 660).

Ferroelectric Measurements: Some LSMO/BTO/LSMO devices were analyzed by PFM in image and spectroscopic modes, by use of an XE7 microscope of Park Systems, with a lock-in amplifier from Stanford Research. An AC modulation voltage of 1.5 V at 7.8 kHz frequency was applied to the conductive tip. The bottom electrode DC bias sweep was performed with a 10 s period.

Supporting Information

Supporting Information is available from the Wiley Online Library or from the author.

Acknowledgements

The authors warmly acknowledge D. Hrabovsky from the "Service Basses Températures" of Sorbonne Université for his tremendous help concerning SMU control. They also thank E. Dandeu from INSP for his precious help at clean room facility and F. Lemarié for the TEM lamella preparation by FIB. The authors acknowledge the "Agence Nationale de la Recherche (ANR)" for funding supports (grant no. ANR-15-CE09-0005-01 and grant no. ANR-11-EQPX-0020).

Conflict of Interest

The authors declare no conflict of interest.

Author Contributions

N.J. conceived and supervised the research project. A.K. carried out most of the measurements. C.H. supervised the growth and L.B. – the lithography. X.P. conducted the TEM experiment. A.K. and N.J. analyzed the data and wrote the manuscript. All authors approved the results.

Data Availability Statement

The data that support the findings of this study are available on request from the corresponding author. The data are not publicly available due to privacy or ethical restrictions.

Keywords

multiferroic tunnel junctions, oxide interfaces, redox processes, resistive switching, second-order memristors, synaptic plasticity

Received: April 13, 2022
Revised: June 18, 2022
Published online: July 13, 2022

[1] S. H. Jo, T. Chang, I. Ebong, B. B. Bhadviya, P. Mazumder, W. Lu, *Nano Lett.* **2010**, *10*, 1297.
[2] L. Chua, *IEEE Trans. Circuit Theory* **1971**, *18*, 507.
[3] D. B. Strukov, G. S. Snider, D. R. Stewart, R. S. Williams, *Nature* **2008**, *453*, 80.
[4] A. L. Hodgkin, A. F. Huxley, *J. Physiol.* **1952**, *117*, 500.
[5] D. M. Kullmann, D. J. Perkei, T. Manabe, R. A. Nicoll, *Neuron* **1992**, *9*, 1175.
[6] J. Rizo, C. Rosenmund, *Nat. Struct. Mol. Biol.* **2008**, *15*, 665.
[7] M. F. Bear, R. C. Malenka, *Curr. Opin. Neurobiol.* **1994**, *4*, 389.
[8] H. Z. Shouval, M. F. Bear, L. N. Cooper, *Proc. Natl. Acad. Sci. USA* **2002**, *99*, 10831.
[9] M. Graupner, N. Brunel, *Proc. Natl. Acad. Sci. USA* **2012**, *109*, 3991.
[10] S.-N. Yang, Y.-G. Tang, R. S. Zucker, *J. Neurophysiol.* **1999**, *81*, 781.
[11] S. Kim, C. Du, P. Sheridan, W. Ma, S. Choi, W. D. Lu, *Nano Lett.* **2015**, *15*, 2203.
[12] C. Du, W. Ma, T. Chang, P. Sheridan, W. D. Lu, *Adv. Funct. Mater.* **2015**, *25*, 4290.
[13] Z. Wang, S. Joshi, S. E. Savel'ev, H. Jiang, R. Midya, P. Lin, M. Hu, N. Ge, J. P. Strachan, Z. Li, Q. Wu, M. Barnell, G.-L. Li, H. L. Xin, R. S. Williams, Q. Xia, J. J. Yang, *Nat. Mater.* **2017**, *16*, 101.
[14] K. Yang, J. Joshua Yang, R. Huang, Y. Yang, *Small Sci.* **2022**, *2*, 2100049.
[15] S. Majumdar, H. Tan, Q. H. Qin, S. van Dijken, *Adv. Electron. Mater.* **2019**, *5*, 1800795.
[16] V. Mikheev, A. Chouprik, Y. Lebedinskii, S. Zarubin, Y. Matveyev, E. Kondratyuk, M. G. Kozodaev, A. M. Markeev, A. Zenkevich, D. Negrov, *ACS Appl. Mater. Interfaces* **2019**, *11*, 32108.
[17] Z. Wen, D. Wu, *Adv. Mater.* **2019**, 1904123.
[18] A. Chanthbouala, V. Garcia, R. O. Cherifi, K. Bouzehouane, S. Fusil, X. Moya, S. Xavier, H. Yamada, C. Deranlot, N. D. Mathur, M. Bibes, A. Barthélémy, J. Grollier, *Nat. Mater.* **2012**, *11*, 860.
[19] D. J. Kim, H. Lu, S. Ryu, C.-W. Bark, C.-B. Eom, E. Y. Tsymbal, A. Gruverman, *Nano Lett.* **2012**, *12*, 5697.
[20] C. Ma, Z. Luo, W. Huang, L. Zhao, Q. Chen, Y. Lin, X. Liu, Z. Chen, C. Liu, H. Sun, X. Jin, Y. Yin, X. Li, *Nat. Commun.* **2020**, *11*, 1439.
[21] Y. Yang, Z. Xi, Y. Dong, C. Zheng, H. Hu, X. Li, Z. Jiang, W.-C. Lu, D. Wu, Z. Wen, *ACS Appl. Mater. Interfaces* **2020**, *12*, 56300.
[22] Z. Xiao, J. Zhao, C. Lu, Z. Zhou, H. Wang, L. Zhang, J. Wang, X. Li, K. Wang, Q. Zhao, Y. Pei, C. Qin, G. Wang, H. Li, R. Guo, J. Chen, D. Ren, X. Yan, *Appl. Phys. Lett.* **2018**, *113*, 223501.
[23] Y. Yang, M. Wu, X. Zheng, C. Zheng, J. Xu, Z. Xu, X. Li, X. Lou, D. Wu, X. Liu, S. J. Pennycook, Z. Wen, *Sci. Adv.* **2021**, *7*, eabh2716.
[24] A. Quindeau, D. Hesse, M. Alexe, *Front. Phys.* **2014**, *2*, 7.
[25] S. Boyn, J. Grollier, G. Lecerf, B. Xu, N. Locatelli, S. Fusil, S. Girod, C. Carrétéro, K. Garcia, S. Xavier, J. Tomas, L. Bellaiche, M. Bibes, A. Barthélémy, S. Saïghi, V. Garcia, *Nat. Commun.* **2017**, *8*, 14736.
[26] T. Yu, F. He, J. Zhao, Z. Zhou, J. Chang, J. Chen, X. Yan, *Sci. China Mater.* **2021**, *64*, 727.
[27] H. Y. Yoong, H. Wu, J. Zhao, H. Wang, R. Guo, J. Xiao, B. Zhang, P. Yang, S. J. Pennycook, N. Deng, X. Yan, J. Chen, *Adv. Funct. Mater.* **2018**, *28*, 1806037.
[28] N. Jedrecy, T. Aghavnian, J.-B. Moussy, H. Magnan, D. Stanescu, X. Portier, M.-A. Arrio, C. Mocuta, A. Vlad, R. Belkhou, P. Ohresser, A. Barbier, *ACS Appl. Mater. Interfaces* **2018**, *10*, 28003.

[29] S. Majumdar, S. van Dijken, *J. Phys. D: Appl. Phys.* **2014**, *47*, 034010.
[30] M. Cesaria, A. P. Caricato, G. Maruccio, M. Martino, *J. Phys.: Conf. Ser.* **2011**, *292*, 012003.
[31] Y.-W. Yin, W.-C. Huang, Y.-K. Liu, S.-W. Yang, S.-N. Dong, J. Tao, Y.-M. Zhu, Q. Li, X.-G. Li, *Adv. Electron. Mater.* **2015**, *1*, 1500183.
[32] W. Huang, Y. Lin, Y. Yin, L. Feng, D. Zhang, W. Zhao, Q. Li, X. Li, *ACS Appl. Mater. Interfaces* **2016**, *8*, 10422.
[33] Q. H. Qin, L. Äkäslompolo, N. Tuomisto, L. Yao, S. Majumdar, J. Vijayakumar, A. Casiraghi, S. Inkinen, B. Chen, A. Zugarramurdi, M. Puska, S. van Dijken, *Adv. Mater.* **2016**, *28*, 6852.
[34] W. Huang, Y.-W. Fang, Y. Yin, B. Tian, W. Zhao, C. Hou, C. Ma, Q. Li, E. Y. Tsymbal, C.-G. Duan, X. Li, *ACS Appl. Mater. Interfaces* **2018**, *10*, 5649.
[35] W. Huang, W. Zhao, Z. Luo, Y. Yin, Y. Lin, C. Hou, B. Tian, C.-G. Duan, X.-G. Li, *Adv. Electron. Mater.* **2018**, *4*, 1700560.
[36] J. Tornos, F. Gallego, S. Valencia, Y. H. Liu, V. Rouco, V. Lauter, R. Abrudan, C. Luo, H. Ryll, Q. Wang, D. Hernandez-Martin, G. Orfila, M. Cabero, F. Cuellar, D. Arias, F. J. Mompean, M. Garcia-Hernandez, F. Radu, T. R. Charlton, A. Rivera-Calzada, Z. Sefrioui, S. G. E. te Velthuis, C. Leon, J. Santamaria, *Phys. Rev. Lett.* **2019**, *122*, 037601.
[37] Q. Zhang, X. Li, J. Zhu, *ACS Appl. Mater. Interfaces* **2021**, *13*, 43641.
[38] N. Jedrecy, V. Jagtap, C. Hebert, L. Becerra, D. Hrabovsky, A. Barbier, X. Portier, *Adv. Electron. Mater.* **2021**, *7*, 2000723.
[39] Y. W. Yin, J. D. Burton, Y.-M. Kim, A. Y. Borisevich, S. J. Pennycook, S. M. Yang, T. W. Noh, A. Gruverman, X. G. Li, E. Y. Tsymbal, Q. Li, *Nat. Mater.* **2013**, *12*, 397.
[40] H. Lu, T. A. George, Y. Wang, I. Ketsman, J. D. Burton, C.-W. Bark, S. Ryu, D. J. Kim, J. Wang, C. Binek, P. A. Dowben, A. Sokolov, C.-B. Eom, E. Y. Tsymbal, A. Gruverman, *Appl. Phys. Lett.* **2012**, *100*, 232904.
[41] L. Chen, Y. Feng, Y. Chen, Y. Chen, R. Liu, D. Pan, P. Wang, Y. Xu, R. Zhang, X. Wang, *Appl. Surf. Sci.* **2020**, *512*, 145707.
[42] S. Slesazeck, T. Mikolajick, *Nanotechnology* **2019**, *30*, 352003.
[43] Y.-M. Kim, A. Morozovska, E. Eliseev, M. P. Oxley, R. Mishra, S. M. Selbach, T. Grande, S. T. Pantelides, S. V. Kalinin, A. Y. Borisevich, *Nat. Mater.* **2014**, *13*, 1019.
[44] S. M. Dudek, M. F. Bear, *Proc. Natl. Acad. Sci. USA* **1992**, *89*, 4363.
[45] A. Kirkwood, M. G. Rioult, M. F. Bear, *Nature* **1996**, *381*, 526.
[46] M. F. Bear, *Proc. Natl. Acad. Sci. USA* **1996**, *93*, 13453.
[47] P. Park, A. Volianskis, T. M. Sanderson, Z. A. Bortolotto, D. E. Jane, M. Zhuo, B.-K. Kaang, G. L. Collingridge, *Philos. Trans. R. Soc., B:* **2014**, *369*, 20130131.
[48] S. Zafar, R. E. Jones, B. Jiang, B. White, P. Chu, D. Taylor, S. Gillespie, *Appl. Phys. Lett.* **1998**, *73*, 175.
[49] D. Zhao, T. Lenz, G. H. Gelinck, P. Groen, D. Damjanovic, D. M. de Leeuw, I. Katsouras, *Nat. Commun.* **2019**, *10*, 2547.
[50] Y. V. Pershin, M. Di Ventra, *Proc. IEEE* **2012**, *100*, 2071.
[51] D. E. Feldman, *Neuron* **2012**, *75*, 556.
[52] C. Luscher, R. C. Malenka, *Cold Spring Harbor Perspect. Biol.* **2012**, *4*, a005710.
[53] L. N. Cooper, Ed., *Theory of Cortical Plasticity*, World Scientific, River Edge, NJ **2004**.
[54] B. D. Philpot, K. K. A. Cho, M. F. Bear, *Neuron* **2007**, *53*, 495.
[55] L. N. Cooper, M. F. Bear, *Nat. Rev. Neurosci.* **2012**, *13*, 798.
[56] E. Bienenstock, L. Cooper, P. Munro, *J. Neurosci.* **1982**, *2*, 32.